

ARTICLE OPEN



Direct visualization of out-of-equilibrium structural transformations in atomically thin chalcogenides

Pawan Kumar^{1,2}, James P. Horwath², Alexandre C. Foucher², Christopher C. Price², Natalia Acero³, Vivek B. Shenoy², Eric A. Stach² and Deep Jariwala¹

Two-dimensional (2D) transition metal dichalcogenides (TMDCs) have been the subject of sustained research interest due to their extraordinary electronic and optical properties. They also exhibit a wide range of structural phases because of the different orientations that the atoms can have within a single layer, or due to the ways that different layers can stack. Here we report a unique study involving direct visualization of structural transformations in atomically thin layers under highly non-equilibrium thermodynamic conditions. We probe these transformations at the atomic scale using real-time, aberration-corrected scanning transmission electron microscopy and observe strong dependence of the resulting structures and phases on both heating rate and temperature. A fast heating rate (25 °C/sec) yields highly ordered crystalline hexagonal islands of sizes of less than 20 nm which are composed of a mixture of 2H and 3R phases. However, a slow heating rate (25 °C/min) yields nanocrystalline and sub-stoichiometric amorphous regions. These differences are explained by different rates of sulfur evaporation and redeposition. The use of non-equilibrium heating rates to achieve highly crystalline and quantum-confined features from 2D atomic layers present a new route to synthesize atomically thin, laterally confined nanostructures and opens new avenues for investigating fundamental electronic phenomena in confined dimensions.

npj 2D Materials and Applications (2020)4:16; <https://doi.org/10.1038/s41699-020-0150-2>

INTRODUCTION

Two-dimensional nanomaterials have received significant attention due to the wide range of exciting properties that they exhibit¹. Transition metal dichalcogenides (TMDCs) have garnered particular interest due to their ability to be utilized in novel electronic device applications^{2,3}. There have been several studies investigating the effect of heat treatments on the structural properties of these systems, but to date these have largely focused on amorphous to crystalline transformation kinetics, point defect kinetics, and dislocation kinetics under equilibrium conditions from ranging ambient to elevated temperatures^{4,5}. Among 2D materials, the TMDCs of Mo and W can exist in multiple phases like 2H, 1T, and 1T', few of them induced by atomic distortions. Furthermore, additional phases, namely 2H' and 3R, are formed by the stacking of 2D layers with different rotational arrangements. In particular, MoS₂—both as a monolayer and in multilayer form—is known to exhibit multiple structural phases. These include the chalcogen distortion-induced 1T phases for both monolayers and thicker crystals and stacking alignment-induced 3R phases in multilayers^{6–9}. The 2H phase is the most thermodynamically stable phase, while the 1T phase and 3R phases are metastable and revert back to the 2H phase over time, or upon application of some form of energy that allows them to overcome the associated activation barrier^{7,10}. Despite the fact that several studies regarding phase identification and evolution have been conducted, the nucleation and formation of metastable phases is still a topic of major debate and discussion^{11–15}. Thus far, in situ electron microscopy studies of TMDCs (such as MoS₂, WS₂, etc.) have largely focused on observations of the kinetics of individual point defects^{16–19}. However, with the rapid growth of interest in the optical, electronic, and mechanical properties of TMDCs^{20–22},

several studies have used in situ scanning transmission electron microscopy (STEM) to document structural transformations under equilibrium conditions^{5,23–27}. In addition, some observations of in situ heterojunction formation and growth have also been made in the same class of materials^{28,29}. These nanoscopic investigations have shown that defects and vacancies form due to the application of multiple types of external stimuli, along with the dynamic migration of transition metal and chalcogen atoms towards favorable grain boundary formations³⁰. There is, however, a lack of understanding on how processing conditions impact atomic scale structure and phase evolution in confined dimensions, including how they lead to the formation of new, metastable phases^{7,8,31}.

Here, we have studied the effect of equilibrium vs. non-equilibrium diffusion conditions during the heating of atomically thin 2D MoS₂ sheets. We find that the effect of heating rate on the morphology of bilayer/few-layer MoS₂ is consistent with the equilibrium bulk binary phase diagram of Mo and S^{32,33}. We see that stoichiometric MoS₂ can phase-separate at low temperatures ($T < 500$ °C) into a two-phase region of Mo + MoS₂ if the sulfur concentration is reduced. At higher temperatures (500 °C $< T < 1000$ °C), the same process leads to a mixture of Mo₂S₃ and 3R phase of MoS₂. Furthermore, if the sulfur content is reduced to below 60 atomic percent, a mixture of Mo and Mo₂S₃ forms. It has been established in the literature that sulfur vacancies, having a low formation energy, are the dominant defect species in few-layer MoS₂³⁴, and that annealing in the 500 °C $< T < 1000$ °C range can lead to loss of sulfur atoms on a time scale of just 30 min³⁵. Moreover, the general phenomena of melting point depression in quantum-confined materials relative to their bulk counterparts is well known^{36,37}. Based on these concepts, we propose that

¹Department of Electrical and Systems Engineering, University of Pennsylvania, Philadelphia, PA 19104, USA. ²Department of Materials Science and Engineering, University of Pennsylvania, Philadelphia, PA 19104, USA. ³Vagelos Integrated Program for Energy Research, University of Pennsylvania, Philadelphia, PA 19104, USA. ✉email: stach@seas.upenn.edu; dmj@seas.upenn.edu

changing the heating rate of a bilayer MoS₂ sample can be used as a proxy to tune the sulfur concentration and change the material structure and morphology of a stoichiometric crystal after synthesis. Direct observation of atomic level diffusion indicates the different crystalline states across the entire thermal diffusion process. Lateral heterophase formation along with statistical observation of particle evolution provides a new pathway for materials engineering in the quantum mechanically relevant size regime³⁸.

RESULTS

Phase transformation processes in equilibrium vs. non-equilibrium heating conditions

Schematics presented in Fig. 1a show the thermal diffusion process in 2D layered MoS₂ crystals, mechanically exfoliated from bulk crystals, when subjected to two different heat treatments: (1) localized, fast heating rates, using embedded heating elements on a chip, which create highly non-equilibrium thermodynamic conditions, and (2) global, slow heating in an equilibrium environment in a hot-walled reactor.

To accomplish these experiments and visualize their atomic structure, exfoliated MoS₂ layers were transferred to heater-embedded TEM grids (Hummingbird Scientific)³⁹. HAADF-STEM images in Fig. 1b, e represent the as-prepared 2D MoS₂ layer before thermal treatment, while Fig. 1c, f shows the transformed MoS₂ after thermal treatment in non-equilibrium and equilibrium conditions, respectively. Since we are using a 200 kV accelerating voltage, it is important to consider the possibility of beam induced transformations in 2D MoS₂ layers at the transformation temperature. After cooling the sample to room temperature, we systematically investigated regions that were not exposed to the electron beam and found that the disintegration process was

identical throughout the sample. This clearly indicates that the primary source of the observed structural changes is the applied thermal stimulus and not the electron beam. Similar results for another set of samples are shown in Supplementary Fig. 1 along with completely unexposed regions after disintegration, Supplementary Fig. 2 to confirm the reproducibility of our experiments. In the case of non-equilibrium (fast) heating, we observe discrete disintegration of continuous, atomically thin and uniform layers of MoS₂ into highly crystalline nanostructures or nanoparticles with lateral dimensions of less than 20 nm, which is within the regime of electronic quantum confinement³⁸. Figure 1d presents examples of nanoscale islands of MoS₂ that form after fast ramping of the flakes shown in Fig. 1b to an elevated temperature (700 °C). Conversely, a slow increase in temperature results in decomposition of the stoichiometric, single crystalline MoS₂ layers into amorphous structures. The sections below discuss the detailed mechanisms and structures observed in each case and correlate them with theoretical insights which account for different evaporation rates of sulfur from the structures.

Macroscopic thermal diffusion in non-equilibrium conditions and the restructuring of heterophase formation

While studies of phase evolution through heating or beam induced transformation have been previously carried out on 2D layered chalcogenides, those studies have been limited to small area, atomic scale investigations which offer limited insight into dynamic phenomena. Large area analysis and observations at different length scales using electron microscopy are lacking. For the case of fast heating, we show this in Fig. 2a, b where a magnification series of images show how the disintegrated portion of an MoS₂ flake taken through a rapid heating cycle develops, including analysis of its atomic structure and crystalline order. It is clear from these images that upon rapid heating the

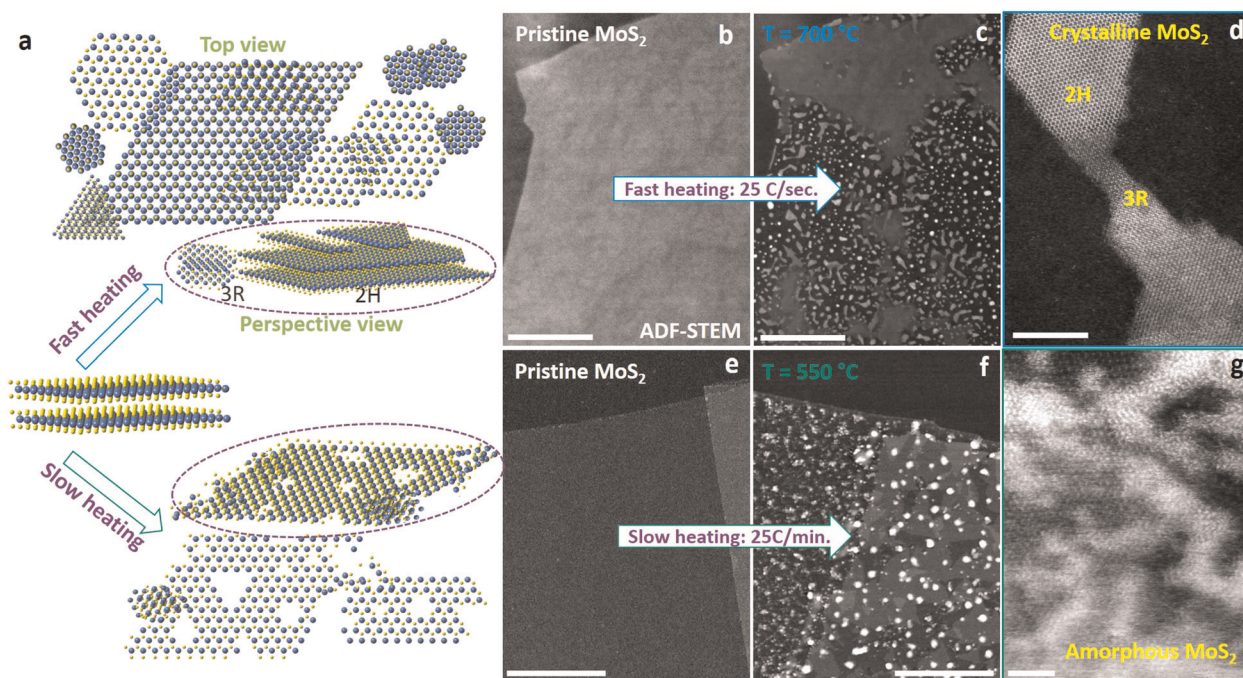


Fig. 1 Direct visualization of diffusion processes for non-equilibrium vs. equilibrium environments. **a** Schematic of the pathways for disintegration vs. decomposition of 2D layers in two discrete environments. **b, e** Scanning transmission electron microscopy (STEM) imaging of pristine bilayer MoS₂, as transferred to the specific microfabricated heating chips with supporting SiN_x membrane underneath for **b** fast heating (non-equilibrium) and **e** slow heating (equilibrium). **c, f** Post-heating images of MoS₂ flakes for **c** fast heating showing nanoscale crystals with uniform intensity contrast and well-defined shapes and **f** slow heating showing disordered spherical structures with non-uniform thickness contrast, as imaged using annular dark field (ADF)-STEM. **d** Fast heating produces ordered nano-crystallites of MoS₂ containing multiple phases while **g** slow heating causes decomposition of MoS₂ leading to amorphous/disordered structures at the atomic scale. STEM images in **d** and **g** taken correspond to sub-regions in **c** and **f**, respectively (scale bars: **b, c:** 200 nm, **d:** 5 nm, **e, f:** 1 μm, **g:** 2 nm).

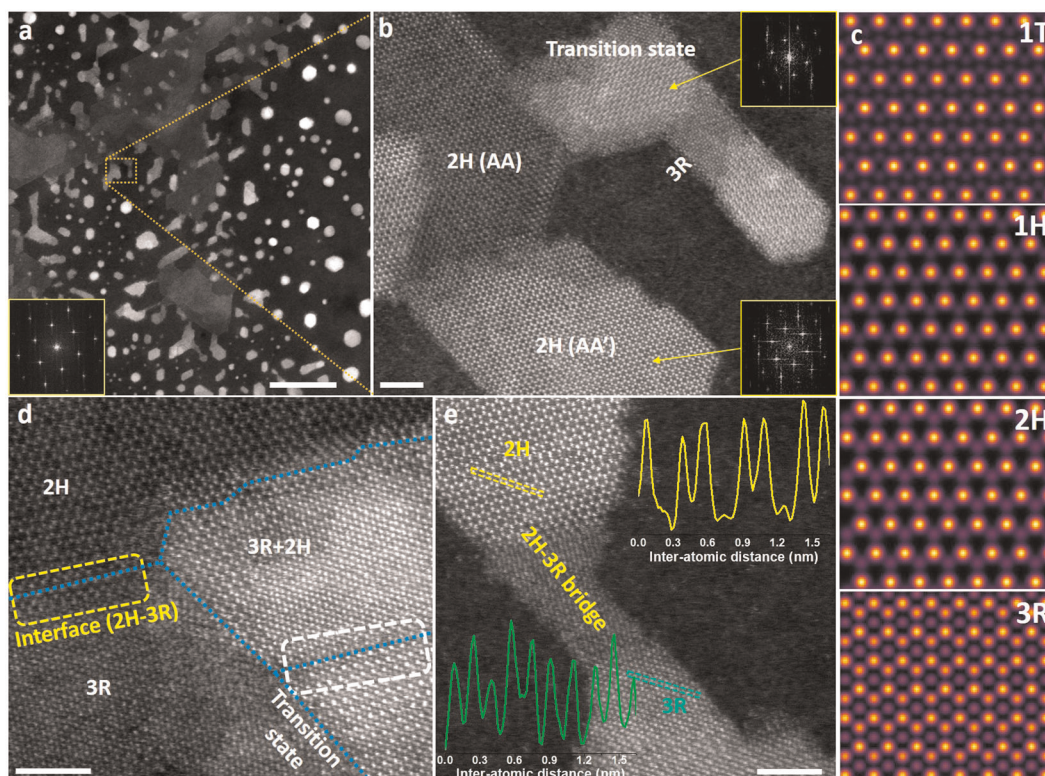


Fig. 2 Ordered MoS₂ nanocrystal formation upon fast (25 °C/sec) in situ heating. **a** Low-magnification ADF-STEM image and Fast Fourier transform (FFT) pattern (inset) shows the high degree of crystallinity of disintegrated MoS₂ from the large 2D sheets. **b** High magnification STEM image of the highlighted boxed region in **a**. The atomic-scale high angle annular dark field (HAADF) STEM image shows the atomic arrangement for different stackings of MoS₂. **c** Simulated STEM images for different poly-phases of MoS₂ to correlate with the experimentally observed atomic level images. **d** Atomically resolved STEM image of a heterojunction region between the 2H and 3R phases, a mixed state (2H + 3R) region, and a transition state of restructured 2H MoS₂. **e** Line profiles across the two different phases (2H and 3R) shows the varying atomic positions in the corresponding structures (scale bars: **a**: 50 nm, **b**, **d**, **e**: 2 nm).

MoS₂ single crystal flake disintegrates into highly crystalline, nanosized islands that retain hexagonal symmetry. This is also evident from the Fast Fourier transform (FFT) patterns in Fig. 2a, b.

Additional atomic resolution STEM images and compositional analysis via energy dispersive X-ray spectroscopy (EDS) are provided in Supplementary Figs. 3 and 4. In addition to observing the highly ordered nature of the disintegrated MoS₂ crystal, we also observe polymorphic phase formation, as highlighted in Fig. 2b, d. FFT and EDS analysis indicated that the crystal symmetry of the 2H phase remained intact. Figure 2b clearly shows the formation of different phases and structural rearrangements of MoS₂ nanostructures, determined to be the 2H and 3R phases. In Fig. 2c, we present image simulations (QSTEM package)⁴⁰ using the same experimental parameters to replicate the observed contrast and structural arrangements seen in the experimental HAADF-STEM images. Only the 2H and 3R phases match with the experimentally observed contrast, and we do not see formation of any other phases, such as 1T and 1T', elsewhere. However, we did find regions interconnecting the 2H and 3R phases which appear as transition states (Fig. 2b, d). Additional analysis of structural arrangement of atoms and stacking order of planes for different phases in these transition regions is provided in Fig. 2d, e. Atomically sharp heterojunction formation is observed at the intersection of the 2H and 3R regions (Fig. 2d) in partially disintegrated regions, suggesting that the equilibrium 2H phase transforms into a metastable 3R phase in certain regions following a fast-thermal treatment. We speculate that the heat supply and dissipation across the flake is non-uniform and the partially disintegrated regions occur when the top atomic layers of the crystal have already disintegrated but the bottom layers have yet

to disintegrate at the time of termination of the experiment. We observe that the occurrence of the 3R phase is strictly limited to fully/partially disintegrated regions of the original 2H-phase continuous crystal. The continuous regions of the original crystal that do not disintegrate all remain in the pure 2H phase, while the partially disintegrated islands show a mixture of 2H and 3R phases (Supplementary Fig. 6). We hypothesize that the 3R phase is formed and stabilized in this case as a result of restacking and vertical mass transport of the van der Waals layers during fast thermolysis of MoS₂.⁹ Atomic scale line profiles along [11 $\bar{2}$ 0] of the two phases have also been plotted in the inset of Fig. 2e. This clearly resolves the atomic locations (peak placement) and chemistry (peak height, equivalent to $\sim Z^2$ contrast) in the two different structures. Additional images and analysis related to the structural model, distributions of 2H and 3R phases, as well as thickness variation after disintegration are provided in Supplementary Figs. 5–7 and Supplementary Video V1.

Coalescence and epitaxial alignment

The above discussion describes the structure of the disintegrated phase upon rapid heating. While this provides new insight into the structural evolution, the dynamics of the transformation are difficult to capture in real-time measurements. This is particularly challenging since, upon reaching the desired temperature, layer disintegration is very rapid and occurs over the acquisition time of only two or three STEM images. We have therefore collected a sequence of bright field TEM images at different times (Fig. 3), at a fixed temperature (650 °C) using a high-frame rate camera (GATAN One-View IS)⁴¹. The sample was slowly heated from room

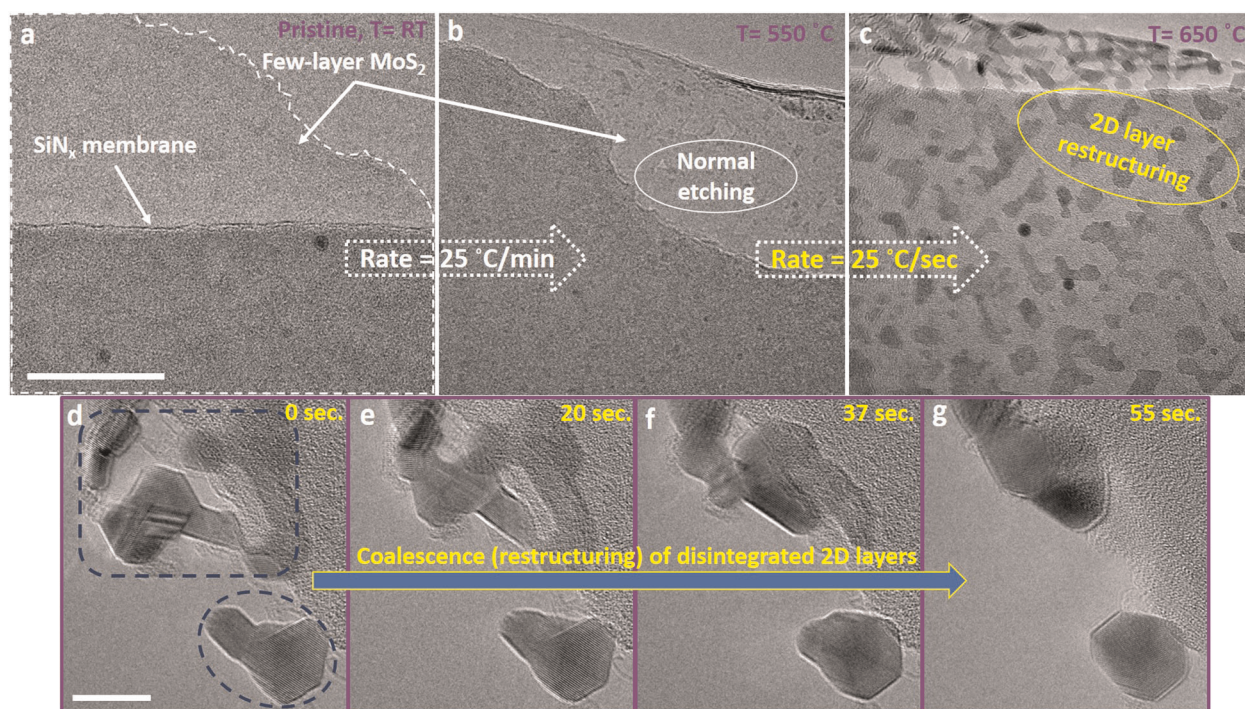


Fig. 3 Real-time observation of few-layer MoS₂ disintegration and subsequent coalescence using BF-TEM imaging. **a** Pristine few-layer MoS₂ at room temperature and the corresponding **b** formation of small etched regions (pits) upon slow (~25°C/min) heating to 550°C. **c** Complete disintegration of same few-layer MoS₂ sample when ramped to 650°C at a fast heating rate (~25°C/sec). **d–g** Sequential snapshots of bright field (BF)-TEM images taken at different times showing further coalescence of the disintegrated MoS₂ (scale bars: **a**: 50 nm, **d**: 10 nm).

temperature to 550°C and then rapidly heated from 550 to 650°C and observed in situ.

Figure 3a, b shows representative images of few-layer MoS₂ when heated to 550°C at a slow ramping rate (25°C/min). Small etch pits form (Fig. 3b), which suggests slow evaporation of chalcogen atoms and associated defect creation in the MoS₂ lattice, see Supplementary Fig. 8 for more details. Upon ramping at an accelerated rate of 25°C/sec from 550 to 650°C, we observe a dramatic transformation of the MoS₂ sheet into disintegrated nanoscopic domains or islands (Fig. 3c, Supplementary Fig. 9). We have also examined the non-irradiated regions (i.e. those not exposed to the electron beam) and find that the MoS₂ sheet undergoes a similar disintegration process after reaching 650°C. Further analysis of sequential phase contrast TEM images (Fig. 3d–g) shows the different stages of coalescence of the MoS₂ nanostructure when held at a constant elevated temperature. Figure 3d–g is a time series of BF-TEM images from the in situ video taken from outside the continuous e-beam exposed region and recorded just after reaching the transformation temperature, 650°C. It is worth noting that with rapid heating these nanostructures spontaneously form on a time scale that is less than the 10 ms/frame of the camera. In contrast, their slow evolution when held at a constant temperature can be captured. As seen in Fig. 3d–g, after 55 s, multiple smaller crystallites of MoS₂ have coalesced into a larger crystal of ~10 nm in diameter with a hexagonal shape. For Fig. 3d–g, the coalescence is prominently visible in the bottom right corner of the image (blue dashed oval). We speculate that the initial disintegration mechanism breaks down the continuous few-layer-thick MoS₂ into regions with geometrical shapes based on energetically favorable facets. As the sample is held at an elevated temperature over time, partial etching ensues resulting in the loss of sulfur atoms via evaporation and the migration of atoms overall. With time, newly formed islands further restructure to reduce their surface energy leading to strongly faceted particles. Figure 3d–g shows that the island

extends only slightly in the lateral dimension as the shape evolves, and that the thickness increases. This is evident from the decreased prominence of lattice fringes and darker contrast in the center of the island. These observations are consistent with well-established theories of particle coalescence, wherein surface diffusion at the point of contact drives restructuring to reduce the total local curvature⁴². It is noteworthy that this thermally driven spontaneous disintegration into nanoscale islands occurs in both free standing as well as substrate supported crystals, as seen in Fig. 3c. While there appears to be a partially connected network of particles in the free-standing region, on the amorphous non-epitaxial SiNx membrane support the particles are isolated and separated into “quantum-dot” sized islands (see Supplementary Fig. 7 for more images and Supplementary video V2 for dynamics of coalescence). The high degree of crystallinity of the lattice both during coalescence (see in situ Supplementary Video V2) and in the sub-10 nm size islands is remarkable and has not been seen before via chemical exfoliation or bottom up synthetic routes for Mo and W chalcogenides, to our knowledge. van der Waals interactions, though weak in nature, can influence growth and epitaxial alignment of the nanoscale islands. Similar van der Waals epitaxy has been exploited for aligned growth of heterostructures on 2D layered materials, as well as TMDCs growth on standard substrates^{43–49}.

Furthermore, upon rapid heating, we observe an interesting epitaxial relationship between fully and partially disintegrated regions of few-layer MoS₂ deposited on an amorphous support layer (SiNx), which is detailed in Fig. 4. High magnification TEM images show that the few-layer MoS₂ goes through a layer-by-layer disintegration, followed by coarsening of the 2D layers. Figure 4a presents a low-magnification TEM image that shows that a large portion of the MoS₂ layer has fully disintegrated into faceted nanostructures, while a small portion in the top-left corner remains only partially disintegrated. Analysis of the geometric alignment of the nanoscale MoS₂ islands indicates that the MoS₂

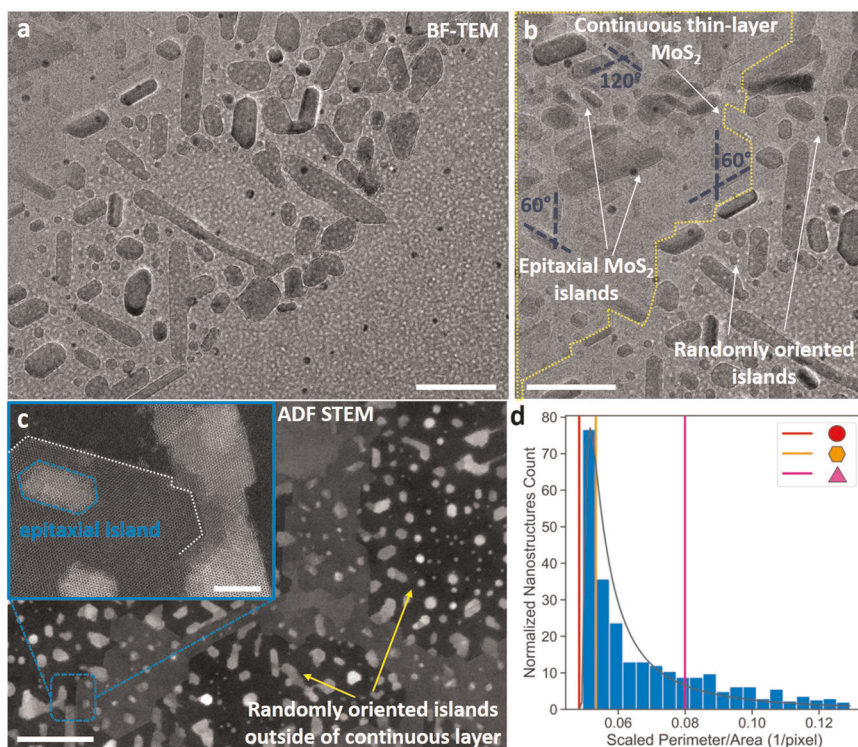


Fig. 4 Epitaxy and orientation during the disintegration of few-layer MoS₂ on in situ microfabricated heating chip. **a** Large area BF-TEM image of the disintegrated portion of MoS₂, where a portion of the flake has completely disintegrated. **b** Partially disintegrated MoS₂ with a supporting, continuous layer of MoS₂ underlying the islands, leading to an epitaxial alignment of the islands over the continuous single crystalline layer. **c** Continuous bilayer MoS₂ disintegrated at 700 °C upon rapid heating shows islands on top of continuous regions as well as fully disintegrated regions. Inset presents an atomic resolution image demonstrating epitaxial alignment in the partially disintegrated region and randomly oriented islands in the completely disintegrated region. **d** Quantitative measurement of island size and shape after the non-equilibrium diffusion. The lines are color coded to island shape in the legend which corresponds to the shape factors of regular polygons with equivalent perimeters (scale bars: **a**, **b**, **c**: 50 nm, **c**—inset: 5 nm).

nanostuctures in the fully disintegrated region do not exhibit any preferential alignment or epitaxy with one another. However, the islands that sit above a continuous single crystalline MoS₂ layer exhibit some preferential alignment (Fig. 4b). We observe that the fully disintegrated MoS₂ nanostructures are transformed into “quantum dot” or faceted nanostructures with random orientations and alignment with respect to one another. In contrast, in the partially disintegrated regions (Fig. 4c, inset) the nanoscale islands maintain perfect epitaxial orientation with the remaining continuous MoS₂ layer. We propose that the disintegration mechanism occurs via point defect formation and aggregation^{17,50} (discussed later in Fig. 6), which originates by preferential sulfur vacancy formation at the surface furthest from the substrate. These surface sulfur vacancies have a lower formation energy than bulk interior sulfur vacancies³⁴. Forming these vacancies primarily at the surface preserves the integrity of vdW interactions between the interior layers, along with the substrate–MoS₂ interactions. Since the sample thickness is significantly less than the mean free path for perpendicular heat transport⁵¹, we expect that quasi-ballistic heat transport perpendicular to the substrate prevents the near-substrate layers from melting and forming a solid–liquid interface first. Although this prior study⁵¹ was conducted at room temperature, the temperature of their experiment was high enough to activate all the acoustic modes which dominate vertical heat transfer⁵², implying a similar phonon mean free path at high temperature. These perpendicular phonons with a high incidence angle can reflect or scatter diffusely at the top surface, which may lead to coupling with in-plane modes and accelerated point defect formation⁵³. Additional characterization details of the

nanoscale islands including information regarding their composition is provided in Supplementary Fig. 10.

Our large area, in situ analysis allows for shape characterization of the population of nanocrystalline islands which form after rapid heating and annealing at 650 °C. The ADF-STEM images such as Fig. 4c are segmented using morphological image filters and a connected components algorithm⁵⁴ to identify each nanoscopic island of MoS₂ from the void or substrate background. The perimeter and area of each island are then measured in terms of number of pixels on the edge and the interior of the island, respectively. We then scale the perimeter of each island to the average (260 pixels) and scale the area by the square of the scale factor. This enables us to use the perimeter to area ratio to characterize the shape of each island, removing the effect of dilation. A histogram of this shape factor is plotted in Fig. 4d for the smallest 775 nanostructures, comprising 90% of the islands detected by the automated segmentation algorithm. The lines overlaid for reference correspond to the shape factors of regular polygons with equivalent perimeters, with the circle having the smallest perimeter/area ratio. The regular hexagon and equilateral triangle are also shown since these shapes have been commonly observed in CVD growth experiments of TMDCs⁵⁵. We see that the majority of the nanoscale islands adopt a shape somewhere between the circle and hexagon, suggesting a rounded hexagonal morphology, broadly consistent with the HAADF-STEM images in Fig. 4. The distribution of island shape factors can be empirically fit by an inverse Gaussian function presented in Eq. (1):

$$f(x, \mu) = \frac{1}{\sqrt{2\pi x^3}} \exp\left(-\frac{(x - \mu)^2}{2x\mu^2}\right)$$

with a shape factor μ of 2.1. A non-normal distribution like this is expected due to the energetic preference for specific edge configurations⁵⁶. The dominance of the hexagonal shape is indicative of a neutral chemical potential environment with a stoichiometric balance and a mixture of chalcogen and metal-terminated edges. Triangular flakes tend to form in extremums of the chemical potential since the edges are either all chalcogen or have a metal-rich zig-zag structure⁵⁷. This is further evidence that the rapid in situ heating rate preserves the composition of the lattice at the initial MoS₂ ratio. This will be discussed in more detail in the Discussion section.

Decomposition and amorphization of MoS₂ under slow, equilibrium heating

The above sections discuss the structural changes that occur during the rapid heating of 2D MoS₂. To isolate the specific effects of the heating rate, we performed a comparative analysis with ex situ, slow heating of the MoS₂ layers on SiNx membranes. A few prior studies have suggested that slow formation of vacancies due to chalcogen removal and migration at elevated temperatures ultimately leads to the formation of voids. Our observations agree with these earlier reports in monolayer to few-layer MoS₂^{17,58}.

Figure 5 presents a detailed analysis for describing these phenomena over a wide range of temperatures and over a large area. Ex situ thermal treatments were carried out in a quartz tube furnace in two different environments (vacuum as well as ultra-high purity Ar gas) using the slow heating rate (25 °C/min), as detailed in the “Methods” section. The slow heating rate and the uniformity of temperature inside the tube furnace makes this an equilibrium heating condition, leading to a fundamentally different disintegration process (called decomposition) than the one observed in the non-equilibrium (rapid heating) case. Slow heating to reach elevated temperatures results in formation and migration of vacancies, starting with the ones that have the lowest formation energies as described in the literature^{30,59,60}. This results in the formation of nanoscale voids in the layers, as shown in Fig. 5a, b. Another distinctive feature of slow heating induced disintegration is that the affected region is localized to high energy or defective regions such as the flake edges, atomic layer step edges, or previously formed defects. Interestingly, areas adjacent to the affected regions maintain high structural integrity and crystalline quality as seen in Fig. 5b (also in Supplementary Fig. 11). This is in sharp contrast to the rapid heating case where the entire flake/crystal simultaneously disintegrates into nanoscale, faceted and highly crystalline islands of stoichiometric MoS₂. Multiple ex situ experiments have been carried out to determine the required thermal conditions to initiate the disintegration process in MoS₂ layers, see Supplementary Fig. 12 for more details. The formation of S vacancies as the temperature is slowly increased leads to a volatile ejection of sulfur compounds, reducing the composition of sulfur in the lattice. This mechanism has been well explored at atomic level in previous reports^{30,61,62}. Since there is a net loss of S from the lattice due to the low energy of vacancy formation and adatom evaporation, this results in a non-stoichiometric decomposition which leads to the formation of nanocrystalline to amorphous MoS₂ or Mo nanocrystals. This can be clearly seen in the atomically resolved HAADF-STEM images as well as the corresponding Fast Fourier Transform (FFT) pattern analyses (Fig. 5c, d, Supplementary Fig. 13). To further clarify our ex situ observations of samples subjected to a slow heating rate, we also carried out the same thermal decomposition for samples held at fixed temperature (525 °C) for different lengths of time (5 and 10 min), as shown in Supplementary Fig. 14. These HAADF-STEM images provide insight into the mechanistic behavior during ex situ thermal decomposition: as the time at 525 °C increases, the formation rate and areal density of pores also increases, which leads to increased void formation in the multilayers and

monolayers (Supplementary Fig. 14c). After 10 min of annealing, bright contrast regions begin to appear, which indicates the formation of Mo/MoS_x nanocrystals along with adjacent regions of amorphized MoS₂. This suggests that the non-stoichiometric disintegration first results in formation of nanocrystalline or amorphous Mo_xS_{2-x} followed by near complete removal of S to form Mo metal nanocrystals. BF-TEM image and compositional analysis are provided in Fig. 5e. To verify that the ex situ, slowly heated samples in a furnace are not affected by trace oxygen or different quality of vacuum in a tube furnace vs. the TEM column, we have also performed control experiments in an inert, ultra-high purity Ar environment (99.995%) where we observed similar etching results (see Supplementary Fig. 15). Here, the increased vapor pressure due to the Ar environment as compared to vacuum raises the disintegration temperature, consistent with our proposed mechanism described below (Fig. 6).

DISCUSSION

During rapid in situ heating, the samples are heated at 25 °C/sec from 500 to 700 °C (Fig. 6a), while during the ex situ experiment shown in Fig. 6b the sample was heated over the same temperature range at a rate of 25 °C/min. The non-equilibrium heating rate (Fig. 6a) causes sulfur vacancies to form quickly, leading to S adatoms on the MoS₂ surface. Over time, collisions between the rapidly expanding adatom population lead to formation of volatile elemental sulfur compounds (S₂, S₈) which leave the surface. However, in only a few seconds, the temperature increases to the point where Mo vacancies begin to form (700 °C), leading to Mo adatoms on the MoS₂ surface. This is assisted by the formation of sulfur vacancy line defects, which reduce the formation energy of a Mo vacancy by increasing the local chemical potential of Mo^{17,50}. The chemical potential imbalance occurs because the diffusion rate of the S vacancies is much faster (barrier of 0.8 eV) than that of the S adatoms (barrier of 1.6 eV), which allows the Mo adatoms to begin forming before the volatile S compounds form and leave the surface^{50,63}. The combination of line defects and sulfur conservation on the surface leads to both void formation and a CVD-type environment for stoichiometric nucleation. CVD growth studies have shown that temperatures of 700–800 °C preferentially lead to vertically stacked MoS₂ growth instead of monolayer growth^{55,63,64}. Random nucleation of these additional layers can lead to a mixture of 2H and 3R stackings, but as voids become larger and multilayer islands become thicker, we expect a shift toward the 3R morphology below 1000 °C, consistent with the bulk phase diagram¹⁷. In contrast, the sample in Fig. 6b spends several minutes in the regime where sulfur vacancies can form but where the temperature is too low to activate Mo adatoms, due to the lower heating rate. The slow heating rate allows for enough time for volatile sulfur compounds to form and leave the surface. This explains the increased depression of the melt process in vacuum vs. the neutral Ar environment, where the reduced vapor pressure accelerates the formation and evolution of the volatile sulfur-rich compounds. This pushes the remaining atomic composition of the lattice into the Mo + MoS₂ or Mo + Mo₂S₃ regimes on the bulk phase diagram. The phase transition temperature is affected by both the vapor pressure and the melting point suppression effect of nanoconfinement. At this reduced sulfur concentration, we expect two-phase regions of Mo and either MoS₂ or Mo₂S₃ to form, as observed in the ex situ heating experiments.

In conclusion, we have performed a detailed analysis of thermal decomposition and disintegration of atomically thin MoS₂ via electron microscopy and spectroscopic analysis. We observe that high heating rates lead to spontaneous disintegration of MoS₂ single crystalline flakes into highly crystalline, nanosized crystals down to 5 nm in diameter, which is in the regime of strong electronic quantum confinement³⁸.

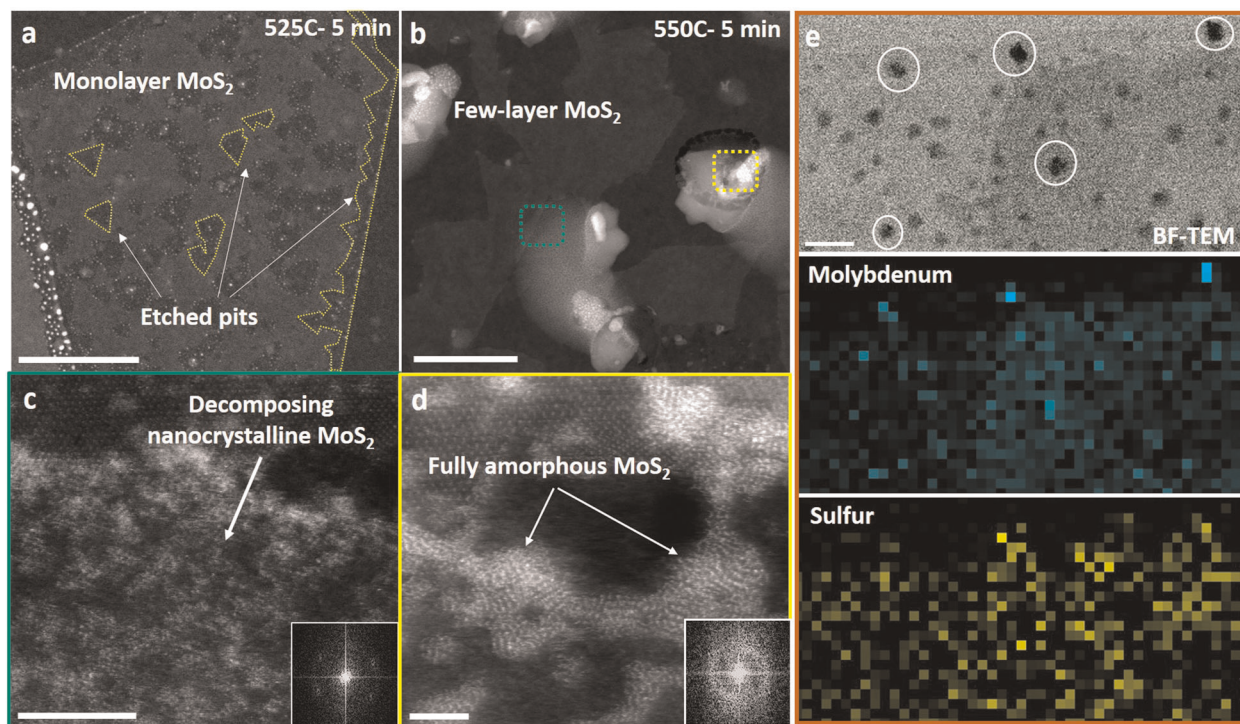


Fig. 5 Ex situ slow-heated (25 °C/min) MoS₂ layers. **a** HAADF-STEM imaging of the MoS₂ heated to 525 °C for 5 min. Triangular etch pits inside the monolayer along with completely etched edges are evident. **b** Images from a few-layer MoS₂ region heated in these same conditions, and at higher magnification. **c** HAADF-STEM image of few-layer MoS₂ heated to 550 °C for 5 min. Nanocrystalline order is evident in corresponding FFT which shows faint, diffused spots (inset). **d** Fully decomposed amorphous MoS₂ along with corresponding FFT inset (550 °C for 5–10 min). FFT patterns (**c** and **d** insets) represent the crystallinity of the corresponding region indicated by the green and yellow dashed rectangular regions marked in **b**. **e** BF-TEM image and corresponding EDX maps of molybdenum (cyan) and sulfur (yellow). The white circles (top) indicate regions of nanocrystal formation which are highly enriched in Mo, ultimately leading to formation of pure Mo metal crystals (scale bars: **a**: 500 nm, **b**: 100 nm, **c**: 5 nm, **d**: 2 nm, **e**: 200 nm).

Furthermore, we observe that this rapid heating leads to a partial disintegration and the subsequent formation of 3R phases in close proximity to the original 2H phase. The nanocrystals in the partially disintegrated region maintain an epitaxial relationship with the underlying layer of MoS₂ while the fully disintegrated regions show random orientation of MoS₂ nanocrystals. In contrast, slow heating results in non-stoichiometric decomposition of MoS₂ single crystals, resulting in first formation of nanocrystalline to amorphous Mo_xS^{2-x} and ultimately Mo metal nanocrystals due to sulfur evaporation. Our study delineates the pathways by which thermally induced disintegration of atomically thin chalcogenides occurs and elucidates the impact of heating rates on the reaction products. This is critical knowledge in applications such as phase change memory, high temperature lubrication, and catalytic processes where MoS₂ can be used. In addition, our studies have shown a unique pathway towards creation of an atomically thin, highly ordered, quantum-dot-like structures via top-down processing which could exhibit unforeseen electronic and optical properties for optoelectronic or catalytic applications.

METHODS

Materials synthesis and experimental procedures

Mechanically exfoliated 2D MoS₂ layers were prepared using the conventional scotch tape method, as described elsewhere⁶⁵. The thickness of the exfoliated layers has been intentionally chosen such that each sample could be reproduced for further thermal diffusion analysis. Exfoliated MoS₂ layers were transferred to the TEM chips/grids with help of a poly-dimethyl siloxane (PDMS) strip, using a dry transfer technique that utilizes micromanipulator stages attached to an optical microscope. After transferring MoS₂ to TEM grids, samples were annealed in a quartz

tube furnace in a closed gas (Ar + H₂) environment to remove all PDMS contaminants. Annealing was performed at 300 °C for 2 h to clean contaminants as well as release the strain developed during the pressure-based transfer method. In situ heating experiments at various temperatures have been done in a specialized TEM holder from Hummingbird Scientific, where a uniquely designed microfabricated heating chip was used. An embedded heating element provides robust stability to perform in situ thermal diffusion analysis at elevated temperatures. Here we have used a microfabricated heating element for heating inside the TEM column (in situ). Because of the very small size of the heating element, we can achieve an ultra-fast heating rate (max 200 °C/s). In contrast, we used quartz tube furnace for our ex situ experiments, which can achieve a maximum of 40 °C/min. We chose a 25 °C/min heating rate, respectively, for all samples in order avoid any overshoot in temperature at the final setpoint. We used the ultra-fast 25 °C/sec heating rate for the in situ heating set-up because during ramping, it takes several seconds (~8 s) to reach the final transformation temperature. This time interval is sufficient to allow for correction of defocusing in the height/image plane of the sample for TEM/STEM imaging, since the rapid heating leads to a change in the vertical position of the sample. Heating calibration was received from the manufacturer to achieve controlled heating based on resistance measurements. We have also verified the heating chip calibrations through Raman Thermometry using Si particles (details provided in Supplementary Information discussion on Raman thermometry along with the temperature calibration curve shown in Supplementary Fig. 16). Equilibrium/slow heating was best-performed ex situ whereas uniform heating (over a few cm² area) has been achieved with a constant heating rate for many different temperatures inside a quartz tube furnace (Lindberg/Blue M mini-mite; Thermo Fisher Scientific). The rough vacuum level of the quartz tube furnace is ~10⁻³ mbar, and the TEM column is at a high vacuum (~10⁻⁶ mbar). Since the vacuum level is directly related to the vapor pressure of the MoS₂, the temperature at which the disintegration phenomena occur are different^{66,67} for in situ vs. ex situ heating, illustrated in Fig. 1. We do not expect any significant differences for slow heating in situ. The in situ conditions with a higher vacuum would

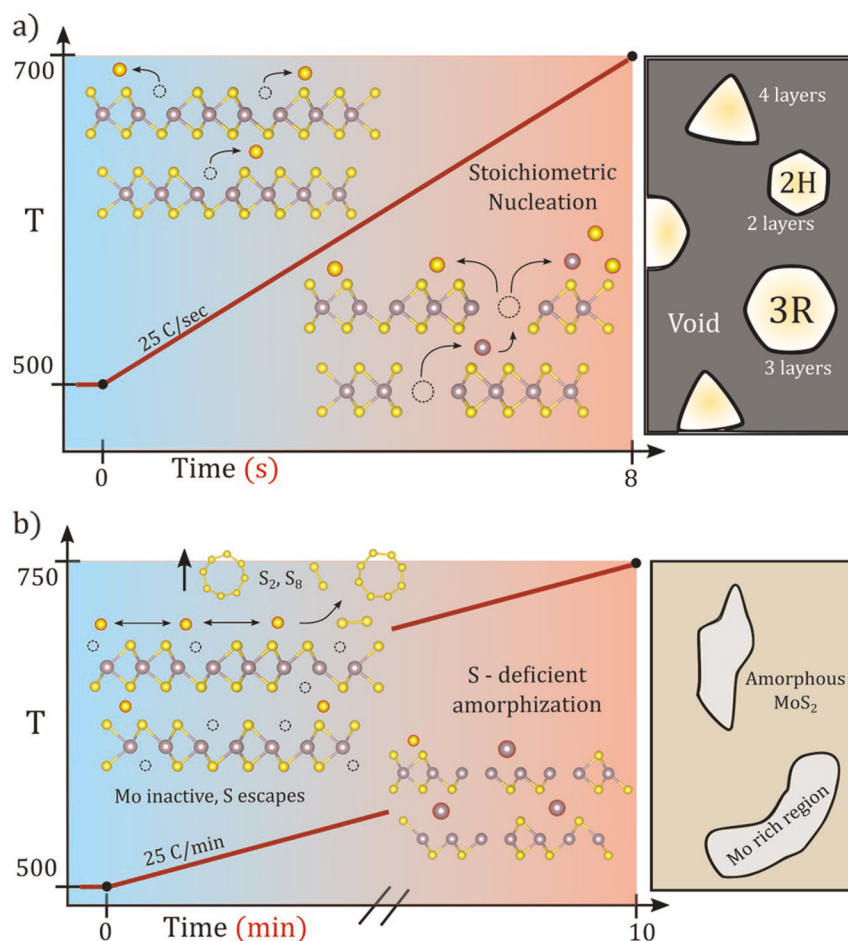


Fig. 6 Comparative, mechanistic descriptions of the slow vs. fast heating induced transformations. **a** Schematic diagram showing that the rapid heating rate leads to the formation of S vacancies and adatoms (yellow circles). Diffusion of S vacancies allows Mo adatoms (purple circles) to recombine with S adatoms before they evolve as volatile elemental products (yellow, S_2 , S_8) and leave the system. **b** In contrast, a slow heating rate prevents Mo adatom formation before S compounds become volatile, preventing subsequent reformation of Mo–S bonds. This results in the system being driven into a two-phase regime composed of Mo-rich regions and amorphous MoS_2 regions.

lead to even more thorough removal of the S as it evaporates during slow heating. Additional conditions used for the in situ and ex situ experiments are mentioned in Supplementary Table 1.

STEM measurements

STEM has been used to measure and analyze all the samples made for in situ and ex situ heating experiments. Two different TEM/STEM systems were used: a JEOL F200 S/TEM and probe-corrected JEOL NEOARM STEM, both operated at 200 kV accelerating voltage. For the JEOL NEOARM STEM, the condenser lens aperture was 40 μm with a camera length of 4 cm for imaging. The probe current was 120 pA. All of the captured TEM images were collected on GATAN IS One View (JEOL F200) and Ultra-scan cameras (JEOL NEOARM), and the STEM images were recorded on the integrated JEOL bright field and annular dark field detectors. In situ TEM videos were acquired on the JEOL F200 using GATAN OneView IS camera at 50 fps with $2k \times 2k$ resolution. Corresponding elemental identification has been performed using a dual detector EDX on the F200 system. Experimentally acquired STEM images are smoothed using the adaptive Gaussian blur function (with radius of 1–2 pixels) available in ImageJ. Image simulation has been performed using QSTEM software⁴⁰. QSTEM is combined with ImageSim for focal series reconstructor and QMB model builder. Adopted parameters for the image simulation were the same as in the experimental conditions for AC-STEM measurements. Image analysis and feature extraction were performed using the open source SciKit-Image⁵⁴ python library.

DATA AVAILABILITY

Most of the datasets generated or analyzed during this study are included in this article (and its Supplementary Information File). Additional findings of this study are available from the corresponding author upon reasonable request.

Received: 21 February 2020; Accepted: 29 April 2020;

Published online: 12 June 2020

REFERENCES

- Novoselov, K. S. et al. Two-dimensional atomic crystals. *Proc. Natl. Acad. Sci. USA* **102**, 10451–10453 (2005).
- Jariwala, D. et al. Emerging device applications for semiconducting two-dimensional transition metal dichalcogenides. *ACS Nano* **8**, 1102–1120 (2014).
- Li, Z. et al. Direct observation of gate-tunable dark trions in monolayer WSe_2 . *Nano Lett.* **19**, 6886–6893 (2019).
- Zhao, X. et al. Healing of planar defects in 2D materials via grain boundary sliding. *Adv. Mater.* **31**, 1900237 (2019).
- Lin, Y.-C. et al. Atomic mechanism of the semiconducting-to-metallic phase transition in single-layered MoS_2 . *Nat. Nanotechnol.* **9**, 391–396 (2014).
- Kappera, R. et al. Phase-engineered low-resistance contacts for ultrathin MoS_2 transistors. *Nat. Mater.* **13**, 1128–1134 (2014).
- Voiry, D. et al. Phase engineering of transition metal dichalcogenides. *Chem. Soc. Rev.* **44**, 2702–2712 (2015).
- Kumar, P. et al. Phase engineering of seamless heterophase homojunctions with co-existing 3R and 2H phases in WS_2 monolayers. *Nanoscale* **10**, 3320–3330 (2018).

9. Ng, H. K. et al. Effects of structural phase transition on thermoelectric performance in lithium-intercalated molybdenum disulfide (Li_xMoS₂). *ACS Appl. Mater. Interfaces* **11**, 12184–12189 (2019).
10. Eda, G. et al. Coherent atomic and electronic heterostructures of single-layer MoS₂. *ACS Nano* **6**, 7311–7317 (2012).
11. Lin, Y. C. et al. Does the metallic 1T phase WS₂ really exist? Preprint at <https://arxiv.org/abs/1907.11398> (2019).
12. Chhowalla, M. et al. The chemistry of two-dimensional layered transition metal dichalcogenide nanosheets. *Nat. Chem.* **5**, 263–275 (2013).
13. Chhowalla, M., Liu, Z. & Zhang, H. Two-dimensional transition metal dichalcogenide (TMD) nanosheets. *Chem. Soc. Rev.* **44**, 2584–2586, <https://doi.org/10.1039/C5CS90037A> (2015).
14. Leng, K. et al. Phase restructuring in transition metal dichalcogenides for highly stable energy storage. *ACS Nano* **10**, 9208–9215 (2016).
15. Chen, Z. et al. Interface confined hydrogen evolution reaction in zero valent metal nanoparticles-intercalated molybdenum disulfide. *Nat. Commun.* **8**, 14548 (2017).
16. Ryu, G. H. et al. Atomic structure and dynamics of self-limiting sub-nanometer pores in monolayer WS₂. *ACS Nano* **12**, 11638–11647 (2018).
17. Chen, Q. et al. Ultralong 1D vacancy channels for rapid atomic migration during 2D void formation in monolayer MoS₂. *ACS Nano* **12**, 7721–7730 (2018).
18. Murthy, A. A. et al. Direct visualization of electric-field-induced structural dynamics in monolayer transition metal dichalcogenides. *ACS Nano* <https://doi.org/10.1021/acsnano.9b06581> (2020).
19. Mendes, R. G. et al. Electron-driven in situ transmission electron microscopy of 2D transition metal dichalcogenides and their 2D heterostructures. *ACS Nano* **13**, 978–995, <https://doi.org/10.1021/acsnano.8b08079> (2019).
20. Jariwala, D. et al. Mixed-dimensional van der Waals heterostructures. *Nat. Mater.* **16**, 170–181 (2017).
21. Sangwan, V. K. et al. Gate-tunable memristive phenomena mediated by grain boundaries in single-layer MoS₂. *Nat. Nanotechnol.* **10**, 403–406 (2015).
22. Oliva, R. et al. Pressure dependence of direct optical transitions in ReS₂ and ReSe₂. *npj 2D Mater. Appl.* **3**, 20 (2019).
23. Chen, J., Ryu, G. H., Sinha, S. & Warner, J. H. Atomic structure and dynamics of defects and grain boundaries in 2D Pd₂Se₃ monolayers. *ACS Nano* **13**, 8256–8264 (2019).
24. Sutter, E. et al. Electron-beam induced transformations of layered tin dichalcogenides. *Nano Lett.* **16**, 4410–4416 (2016).
25. Lin, J. et al. Novel Pd₂Se₃ two-dimensional phase driven by interlayer fusion in layered PdSe₂. *Phys. Rev. Lett.* **119**, 016101 (2017).
26. Elibol, K. et al. Atomic structure of intrinsic and electron-irradiation-induced defects in MoTe₂. *Chem. Mater.* **30**, 1230–1238 (2018).
27. Lehnert, T. et al. Electron-beam-driven structure evolution of single-layer MoTe₂ for quantum devices. *ACS Appl. Nano Mater.* **2**, 3262–3270 (2019).
28. Tai, K. L. et al. Atomic-scale fabrication of in-plane heterojunctions of few-layer MoS₂ via in situ scanning transmission electron microscopy. *Small* <https://doi.org/10.1002/sml.201905516> (2019).
29. Zuluaga, S. et al. Two-dimensional PdSe₂-Pd₂Se₃ junctions can serve as nanowires. *2D Mater.* **5**, 035025 (2018).
30. Chen, J. et al. In situ high temperature atomic level dynamics of large inversion domain formations in monolayer MoS₂. *Nanoscale* **11**, 1901–1913 (2019).
31. Zhao, W. et al. Energetics and kinetics of phase transition between a 2H and a 1T MoS₂ monolayer—a theoretical study. *Nanoscale* **9**, 2301–2309 (2017).
32. Tesfaye, F. et al. *Phase Equilibria and Thermochemistry of Selected Sulfide Systems in the Pyrometallurgy of Ni and Cu*. Aalto University publication series SCIENCE + TECHNOLOGY (2012).
33. Johnson, W. B. et al. A molybdenum sulfur binary phase diagram. *Scr. Metall.* **17**, 919–922, [https://doi.org/10.1016/0036-9748\(83\)90262-4](https://doi.org/10.1016/0036-9748(83)90262-4) (1983).
34. Komsa, H.-P. et al. Native defects in bulk and monolayer MoS₂ from first principles. *Phys. Rev. B* **91**, 125304 (2015).
35. Pitthan, E. et al. Annealing response of monolayer MoS₂ grown by chemical vapor deposition. *ECS J. Solid State Sci. Technol.* **8**, P267–P270, <https://doi.org/10.1149/2.0061904jss> (2019).
36. Couchman, P. R. et al. Thermodynamic theory of size dependence of melting temperature in metals. *Nature* **269**, 481–483 (1977).
37. Lai, S. L. et al. Size-dependent melting properties of small tin particles: nanocalorimetric measurements. *Phys. Rev. Lett.* **77**, 99–102 (1996).
38. Price, C. C. et al. Engineering zero-dimensional quantum confinement in transition-metal dichalcogenide heterostructures. *ACS Nano* **13**, 8303–8311, (2019).
39. Scientific, H. *MEMS Heating + Biasing*, <http://hummingbirdscientific.com/products/heating-biasing/>.
40. Faculty of Mathematics and Natural Sciences. *QSTEM: Quantitative TEM/STEM Simulations*, https://www.physics.hu-berlin.de/en/sem/software/software_qstem (2002).
41. AMETEK; GATAN. *OneView Camera*. <https://www.gatan.com/products/tem-imaging-spectroscopy/oneview-camera>.
42. Kingery, W. D. et al. *Introduction to Ceramics*. (Wiley, 1976).
43. Li, H. et al. Epitaxial growth of two-dimensional layered transition-metal dichalcogenides: growth mechanism, controllability, and scalability. *Chem. Rev.* **118**, 6134–6150 (2018).
44. Kumar, P. et al. Effect of Sulfur evaporation rate on screw dislocation driven growth of MoS₂ with high atomic step density. *Cryst. Growth Des.* **16**, 7145–7154 (2016).
45. Hu, Z. et al. Two-dimensional transition metal dichalcogenides: interface and defect engineering. *Chem. Soc. Rev.* **47**, 3100–3128 (2018).
46. Dumcenco, D. et al. Large-area epitaxial monolayer MoS₂. *ACS Nano* **9**, 4611–4620 (2015).
47. Duan, X. et al. Lateral epitaxial growth of two-dimensional layered semiconductor heterojunctions. *Nat. Nanotechnol.* **9**, 1024–1030 (2014).
48. Fu, D. et al. Molecular beam epitaxy of highly crystalline monolayer molybdenum disulfide on hexagonal boron nitride. *J. Am. Chem. Soc.* **139**, 9392–9400 (2017).
49. Koma, A. et al. Fabrication and characterization of heterostructures with sub-nanometer thickness. *Microelectron. Eng.* **2**, 129–136 (1984).
50. Le, D. et al. Single-layer MoS₂ with sulfur vacancies: structure and catalytic application. *J. Phys. Chem. C* **118**, 5346–5351 (2014).
51. Sood, A. et al. Quasi-ballistic thermal transport across MoS₂ thin films. *Nano Lett.* **19**, 2434–2442 (2019).
52. Carvalho, B. R. et al. Intervalley scattering by acoustic phonons in two-dimensional MoS₂ revealed by double-resonance Raman spectroscopy. *Nat. Commun.* **8**, 14670 (2017).
53. Malhotra, A. et al. Impact of phonon surface scattering on thermal energy distribution of Si and SiGe nanowires. *Sci. Rep.* **6**, 25818 (2016).
54. van der Walt, S. et al. scikit-image: image processing in Python. *PeerJ* **2**, e453–e453 (2014).
55. Ye, H. et al. Toward a mechanistic understanding of vertical growth of van der Waals stacked 2D materials: a multiscale model and experiments. *ACS Nano* **11**, 12780–12788 (2017).
56. Chen, Q. et al. Atomically flat zigzag edges in monolayer MoS₂ by thermal annealing. *Nano Lett.* **17**, 5502–5507 (2017).
57. Wang, S. et al. Shape evolution of monolayer MoS₂ crystals grown by chemical vapor deposition. *Chem. Mater.* **26**, 6371–6379 (2014).
58. Xu, W. et al. In-situ atomic-scale observation of irradiation-induced void formation. *Nat. Commun.* **4**, 2288 (2013).
59. Kumar, P. et al. Scalable faceted voids with luminescent enhanced edges in WS₂ monolayers. *Nanoscale* **10**, 16321–16331 (2018).
60. Zhou, W. et al. Intrinsic structural defects in monolayer molybdenum disulfide. *Nano Lett.* **13**, 2615–2622 (2013).
61. Li, L. et al. Role of sulfur vacancies and undercoordinated Mo regions in MoS₂ nanosheets toward the evolution of hydrogen. *ACS Nano* **13**, 6824–6834 (2019).
62. Chen, P. et al. Thermal degradation of monolayer MoS₂ on SrTiO₃ supports. *J. Phys. Chem. C* **123**, 3876–3885 (2019).
63. Gong, Y. et al. Vertical and in-plane heterostructures from WS₂/MoS₂ monolayers. *Nat. Mater.* **13**, 1135–1142 (2014).
64. Kumar, P. et al. Horizontally and vertically aligned growth of strained MoS₂ layers with dissimilar wetting and catalytic behaviors. *CrystEngComm* **19**, 5068–5078 (2017).
65. Li, H. et al. Preparation and applications of mechanically exfoliated single-layer and multilayer MoS₂ and WSe₂ Nanosheets. *Acc. Chem. Res.* **47**, 1067–1075 (2014).
66. Li, S. et al. Vapour–liquid–solid growth of monolayer MoS₂ nanoribbons. *Nat. Mater.* **17**, 535–542 (2018).
67. Frankel, H. E. Effects of vacuum on materials. In *ESRO Environment and their Role in Spacecraft Technology* Vol. 1, 137–181 (1969).

ACKNOWLEDGEMENTS

This work was carried out in part at the Singh Center for Nanotechnology at the University of Pennsylvania which is supported by the National Science Foundation (NSF) National Nanotechnology Coordinated Infrastructure Program grant NNCI-1542153. D.J., E.A.S., and P.K. acknowledge primary support for this work from University of Pennsylvania Materials Research Science and Engineering Center (MRSEC) seed grant supported by the National Science Foundation (DMR-1720530) and NSF DMR Electronic Photonic and Magnetic Materials (EPM) core program grant (DMR-1905853). N.A. and D.J. acknowledge support from Vagelos Integrated Program in Energy Research at University of Pennsylvania as well as the Center for Undergraduate Research and Fellowships at Penn. D.J. also acknowledges support for this work by the U.S. Army Research Office under contract number W911NF1910109. J.P.H. and E.A.S. acknowledge support through the National Science Foundation, Division of Materials Research, Metals and Metallic Nanostructures Program under Grant 1809398. A.C.F. and E.A.S. would like to acknowledge the Vagelos Institute for Energy Science and Technology at the University of

Pennsylvania for a graduate fellowship. C.C.P. and V.B.S. acknowledge support from NSF grant CMMI-1727717. The authors thank Douglas Yates and Jamie Ford in the Singh Center for Nanotechnology for help with the TEM/STEM measurements.

AUTHOR CONTRIBUTIONS

P.K., E.A.S., and D.J. conceived and planned the project; P.K. prepared the samples with assistance from N.A.; P.K. performed all in situ and ex situ heating and microscopy imaging experiments with assistance from J.P.H. on temperature calibration and A.C.F. on HAADF imaging; P.K. and J.P.H. completed QSTEM simulation and crystal maker image analysis; J.P.H. performed the particle size and shape distribution analysis; C.C.P. and V.B.S. provided theoretical support and mechanistic understanding of the observed experimental phenomena; P.K., E.A.S., and D.J. wrote the whole manuscript with contribution of all co-authors.

COMPETING INTERESTS

The authors declare no competing interests.

ADDITIONAL INFORMATION

Supplementary information is available for this paper at <https://doi.org/10.1038/s41699-020-0150-2>.

Correspondence and requests for materials should be addressed to E.A.S. or D.J.

Reprints and permission information is available at <http://www.nature.com/reprints>

Publisher's note Springer Nature remains neutral with regard to jurisdictional claims in published maps and institutional affiliations.



Open Access This article is licensed under a Creative Commons Attribution 4.0 International License, which permits use, sharing, adaptation, distribution and reproduction in any medium or format, as long as you give appropriate credit to the original author(s) and the source, provide a link to the Creative Commons license, and indicate if changes were made. The images or other third party material in this article are included in the article's Creative Commons license, unless indicated otherwise in a credit line to the material. If material is not included in the article's Creative Commons license and your intended use is not permitted by statutory regulation or exceeds the permitted use, you will need to obtain permission directly from the copyright holder. To view a copy of this license, visit <http://creativecommons.org/licenses/by/4.0/>.

© The Author(s) 2020